The current issue and full text archive of this journal is available at
www.emeraldinsight.com/0961-5539.htm

Numerical analysis for the flow past a porous square cylinder based on the stress-jump interfacial-conditions

Xiaobing Chen, Peng Yu and S.H. Winoto
Department of Mechanical Engineering, National University of Singapore, Singapore, and
Hong-Tong Low
Division of Bioengineering, National University of Singapore, Singapore

Received 15 January 2007
Revised 7 May 2007
Accepted 7 June 2007

Abstract

Purpose – The purpose of this paper is to report on the flow past a porous square cylinder, implementing the stress jump treatments for the porous-fluid interface.

Design/methodology/approach – The numerical method was developed for flows involving an interface between a homogenous fluid and a porous medium. It is based on the finite volume method with body-fitted and multi-block grids. The Brinkman-Forcheimmer extended model was used to govern the flow in the porous medium region. At its interface, a shear stress jump that includes the inertial effect was imposed, together with a continuity of normal stress.

Findings – The present model is validated by comparing with those for the flow around a solid circular cylinder. Results for flow around porous square cylinder are presented with flow configurations for different Darcy number, 10^{-2} to 10^{-5}, porosity from 0.4 to 0.8, and Reynolds number 20 to 250. The flow develops from steady to unsteady periodic vortex shedding state. It was found that the stress jump interface condition can cause flow instability. The first coefficient β has a more noticeable effect whereas the second coefficient β_1 has very small effect, even for $Re = 200$. The effects of the porosity, Darcy number, and Reynolds number on lift and drag coefficients, and the length of circulation zone or shedding period are studied.

Originality/value – The present study implements the numerical method based on finite volume method with a collocated variable arrangement to treat the stress jump condition.

Keywords Porous materials, Fluid flow, Fluid power cylinders, Numerical analysis

Paper type Research paper

Nomenclature

A	= discretization coefficients using SIMPLEC method	K	= permeability of porous medium (m^2)
C_d	= drag coefficient	k_f	= fluid thermal conductivity
C_F	= Forchheimer coefficient	k_{eff}	= effective thermal conductivity of porous media
C_l	= lift coefficient		
Da	= Darcy number	n	= unit vector along normal direction of the interface
e_x	= unit vector along x-axis		
e_y	= unit vector along y-axis	Pr	= fluid Prandtl number
H	= side length of the square cylinder (m)	p, p_f	= local average and intrinsic average pressure (Pa)

International Journal of Numerical Methods for Heat & Fluid Flow
Vol. 18 No. 5, 2008
pp. 635-655

0961-5539
DOI 10.1108/09615530810879756

Re = Reynolds number
$\mathbf{S}$ = surface vector
t = unit vector along tangential direction to the interface, time
U = incoming flow velocity
u, v = velocity components along x- and y-axes, respectively
x, y = Cartesian coordinates

Greek symbols
β = stress jump parameter
β_1 = stress jump parameter related to inertia
ε = porosity
ε_c = convergence error
μ = dynamic viscosity
λ = interpolation factor
ρ = fluid density
φ = general dependent variable
$\Delta\Omega$ = finite volume of the control cell

Subscripts
fluid = fluid part
eff = effective value for porous media
e = east
n = north
w = west
s = south
interface = interface value
p = control volume center point
porous = porous part
t = tangential direction to the interface

Superscripts
c = convection effect
d = diffusion effect
m = iteration time step
n = iteration step for each time level

1. Introduction

The flow past bluff bodies, especially cylinders, has been investigated extensively for a long time. Most of these studies concentrated on the circular cylinder case under free flow conditions as reviewed by Williamson (1996) and Zdravkovich (1997). However, the research on square cylinder case has not been investigated to the same extent, although it plays a dominant role in many technical applications, such as building aerodynamics, as studied by Davis and Moore (1982), Davis *et al.*(1984), Franke *et al.* (1990), Klekar and Patankar (1992) and Suzuki *et al.* (1993). They have provided numerical and experimental data about lift coefficient, drag coefficient, base pressure and Strouhal frequency for a range of Reynolds number up to 2,800.

However, most of the studies focused on the flow past impermeable bodies, and the flow behind a porous body has not been broadly investigated. Most of the research about flow behind porous bodies concentrated on the steady-state convection heat transfer phenomena (Huang and Vafai, 1993; Martin *et al.*, 1998). For unsteady problems, the flow over a circular cylinder with surface suction and blowing was theoretically investigated by Cohen (1991). He derived a model for *St-Re* relationship by order of magnitude estimation. Ling *et al.* (1993) numerically verified this model for flow over a square cylinder and obtained a similar trend between Strouhal and Reynolds numbers. Their research does not consider porous flow. Jue (2004) simulated vortex shedding behind a porous square cylinder by finite element method, for which the details are given later.

The porous-interface conditions are essential for solving the governing equations in the fluid and porous regions as they are applied at the interface to close the two sets of equations.

Beavers and Joseph (1967) proposed a semi-empirical slip boundary condition. Neale and Nader (1974) assumed continuous boundary conditions in both velocity and stress. Kim and Choi (1996) used an effective viscosity in the formulation of the continuous stress condition at the interface. By matching both velocity and stress, Vafai and Kim (1990) provided an exact solution for the fluid flow at the interface, which includes the inertial and boundary effects.

A stress jump condition at the interface was deduced by Ochoa-Tapia and Whitaker (1995a, b) based on the non-local form of the volume averaged method. Based on the Forchheimer equation with the Brinkman correction and the Navier-Stokes equations, Ochoa-Tapia and Whitaker (1998) developed another stress jump condition which includes the inertial effects. Two coefficients appear in this jump condition: one is associated with an excess viscous stress and the other is related to an excess inertial stress.

Numerical solutions for the coupled viscous and porous flows have been attempted by Gartling *et al.* (1996), Silva and de Lemos (2003), Costa *et al.* (2004), Jue (2004) and Betchen *et al.* (2006). Different types of interfacial conditions between a porous medium and a homogenous fluid have been proposed; and found to have a pronounced effect on the velocity field as shown by Alazmi and Vafai (2001). Although the one-domain approach, or a continuity of both velocity and stress, is easier to implement, the stress jump conditions have been commonly adopted.

The implementation of the numerical methodology on the stress jump condition based on Ochoa-Tapia and Whitaker (1995a, b) can be found in the work of Silva and de Lemos (2003). In their study, only the jump in shear stress was included and no special treatment on velocity derivatives was mentioned. However, for flow in general, it is needed to consider how to formulate the velocity derivatives at the interface. Also, for the two-dimensional problem, the normal stress condition is needed to close the sets of equations.

Jue (2004) simulated vortex shedding behind a porous square cylinder by finite element method. In his study, a general non-Darcy porous media model was applied to describe the flows both inside and outside the cylinder. A harmonic mean was used to treat the sudden change between the fluid and porous medium. He also pointed out that Darcy number demonstrates more influence on the flow field than porosity does.

The objective of the present study was to implement the numerical method based on finite volume method with a collocated variable arrangement to treat the stress jump condition given by Ochoa-Tapia and Whitaker (1998), which includes the inertial effects. The numerical method was developed for flows involving an interface between a homogenous fluid and a porous medium and it is based on the finite volume method with body-fitted and multi-block grids. The same interface conditions for steady flow around a porous square cylinder has been analysed by Yu *et al.* (2007), only for $Re = 20$. In our simulation, steady and unsteady flow around a porous square cylinder are both considered, with Re up to 250. The stress jump interface condition effects to the drag coefficient, lift coefficient and shedding period are also studied.

2. Mathematical model

A two-dimensional, laminar and incompressible flow past a square cylinder is considered here (Figure 1(a)). The fluid is Newtonian and the properties of the fluid are assumed to be constant.

The governing equations for a homogenous fluid region, using vector form, can be written as:

$$\nabla \cdot \vec{u} = 0 \tag{1}$$

$$\rho \frac{\partial u}{\partial t} + \nabla \cdot (\rho \vec{u}\vec{u}) = -\nabla p + \mu \nabla^2 \vec{u} \tag{2}$$

where p is the pressure; ρ is the mass density of the fluid; and μ is the fluid dynamic viscosity.

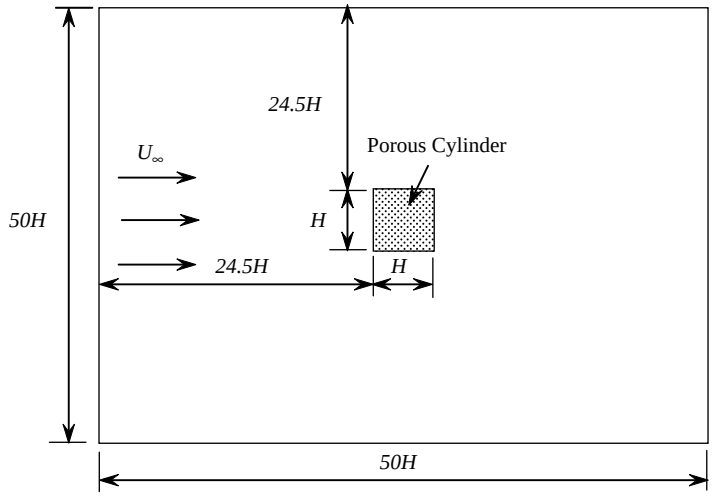

(a) Computational domain

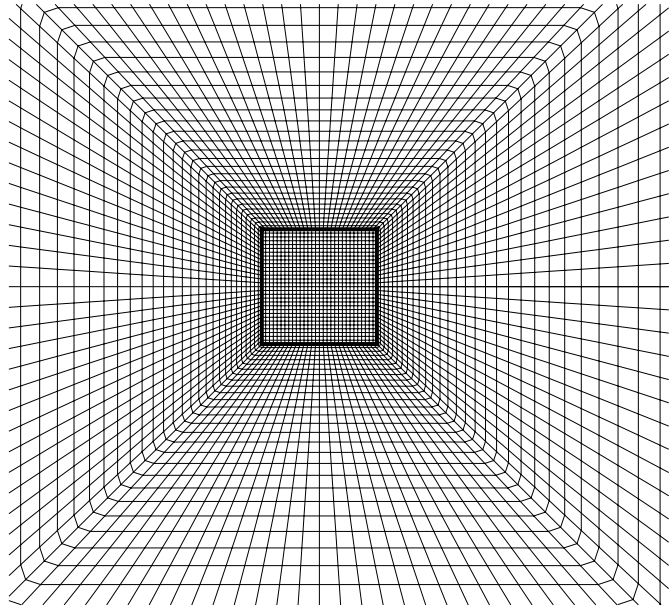

(b) Mesh illustration

Figure 1.
Schematic of flow past a porous square cylinder

The porous medium is considered to be rigid, homogeneous and isotropic; and saturated with the same single-phase fluid as that in the homogenous fluid region. Considering viscous and inertial effects, the governing equations for porous region based on Darcy-Brinkman-Forchheimer extended model can be expressed as with Hsu and Cheng (1990) and Nithiarasu *et al.* (2002):

$$\nabla \cdot \vec{u} = 0 \tag{3}$$

$$\underbrace{\rho \frac{\partial u}{\partial t}}_{\text{Unsteady term}} + \underbrace{\nabla \cdot \left(\frac{\rho \vec{u} \vec{u}}{\varepsilon} \right)}_{\text{Convective term}} = \underbrace{-\nabla(\varepsilon p^*)}_{\text{Pressure term}} + \underbrace{\mu \nabla^2 \vec{u}}_{\text{Brinkman term}} - \underbrace{\frac{\mu \varepsilon}{K} \vec{u}}_{\text{Darcy term}} - \underbrace{\frac{\rho \varepsilon C_F |\vec{u}|}{\sqrt{K}} \vec{u}}_{\text{Forchheimer term}} \tag{4}$$

where $\vec{u}$ is the local average velocity vector (Darcy velocity); p^* is the intrinsic average pressure; μ is the fluid dynamic viscosity; ε is the porosity; K is the permeability; and C_F is Forchheimer coefficient. Note that throughout the paper, viscosity means dynamic viscosity of the fluid but not the effective (Brinkman) viscosity. The superscript * denotes the intrinsic average. The local average and intrinsic average can be linked by the Dupuit-Forchheimer relationship, for example, $p = \varepsilon p^*$.

At the interface between the homogeneous fluid and porous medium regions, additional boundary conditions must be applied to couple the flows in the two regions. In the present study, the stress jump condition of Ochoa-Tapia and Whitaker (1998) is applied:

$$\frac{\mu}{\varepsilon} \left. \frac{\partial u_t}{\partial n} \right|_{\text{Porous}} - \mu \left. \frac{\partial u_t}{\partial n} \right|_{\text{Fluid}} = \beta \frac{\mu}{\sqrt{K}} \left. u_t \right|_{\text{Interface}} + \beta_1 \rho u_t^2 \tag{5}$$

where in the porous medium region, u_t is the Darcy velocity component parallel to the interface aligned with the direction t and normal to the direction n while in the homogenous fluid region u_t is the fluid velocity component parallel to the interface; β and β_1 are adjustable parameters which account for the stress jump at the interface.

Ochoa-Tapia and Whitaker (1998) derived analytical expressions for parameters β and β_1 which indicate their dependence on permeability and porosity. They concluded that these two parameters are both of order one. Ochoa-Tapia and Whitaker (1995b) experimentally determined that β varies from + 0.7 to −1.0 for different materials with permeability varying from 15×10^{-6} to 127×10^{-6} in.^{2} and average pore size from 0.016 to 0.045 in. There is presently no experimental data for β_1. It is not known how much the two parameters may change from one type of interface to another; and it is assumed in this study that the changes should be in the same range as those for different types of materials. Thus, for the purpose of demonstrating the implementation of the present formulation, both β and β_1 are varied in the range −0.7 to +0.7 in the present study.

In addition to equation (5), the continuity of velocity and normal stress prevailing at the interface is given by:

$$\vec{u}|_{\text{Fluid}} = \vec{u}|_{\text{Porous}} = \vec{v}_{\text{Interface}} \tag{6}$$

$$\frac{\mu}{\varepsilon} \left. \frac{\partial u_n}{\partial n} \right|_{\text{Porous}} - \mu \left. \frac{\partial u_n}{\partial n} \right|_{\text{Fluid}} = 0 \tag{7}$$

where in the porous medium region, u_n is the Darcy velocity component normal to the interface; and in the homogenous fluid region, u_n is the fluid velocity component normal to the interface. By combining with the appropriate boundary conditions of the composite region, equations (1)-(7) can be used to simulate the flow in a system composed of a porous medium and a homogenous fluid.

3. Discretization of the governing equations

3.1 Homogenous fluid region

A typical control volume is shown in Figure 2. For a general dependent variable φ, a final discrete form over the control volume can be written as:

$$F_e + F_w + F_n + F_s = S \tag{8}$$

where F_e, F_w, F_n and F_s are the overall fluxes (including both convection and diffusion) of φ at faces e, w, n, s, which denote east, west, north, and south of the control volume; and S is the source term. The detailed numerical methodology for obtaining the convective flux (F_e^c, F_w^c, F_n^c, and F_s^c) and diffusive flux (F_e^d, F_w^d, F_n^d, and F_s^d) are given in Ferziger and Perić (1999).

With the midpoint rule approximation, the convective flux at face east can be calculated as:

$$F_e^c = \int_{\mathbf{S}_e} \rho\varphi\vec{u}\cdot\vec{n}\mathrm{d}\mathbf{S} \approx m_e\varphi_e \tag{9}$$

where m_e is the mass flux cross the surface e; $\mathbf{S}_e$ is the surface area of face e; and φ_e is the value of φ at the center of the cell face. m_e and $\mathbf{S}_e$ can be calculated as:

$$m_e = \rho_e(\mathbf{S}^x u + \mathbf{S}^y v)_e, \quad \mathbf{S}_e = \sqrt{\left(\mathbf{S}_e^x\right)^2 + \left(\mathbf{S}_e^y\right)^2} \tag{10}$$

where u and v are the velocity components in the x and y directions; $\mathbf{S}^x$ and $\mathbf{S}^y$ are the surface vector components.

To avoid the non-orthogonal effect, the midpoint rule with the deferred correction term (Muzaferija, 1994) applied to the integrated diffusive flux is given by:

$$F_e^d = \mu_e\left(\frac{\partial\varphi}{\partial \mathrm{n}}\right)_e \mathbf{S}_e = \mu_e\mathbf{S}_e\left(\frac{\partial\varphi}{\partial\xi}\right)_e + \mu_e\mathbf{S}_e\left[\overline{\left(\frac{\partial\varphi}{\partial \mathrm{n}}\right)}_e - \overline{\left(\frac{\partial\varphi}{\partial\xi}\right)}_e\right]^{\mathrm{old}} \tag{11}$$

If an implicit flux approximation of the term $(\partial\varphi/\partial\xi)_e$ is applied, the final expression of equation (11) then becomes:

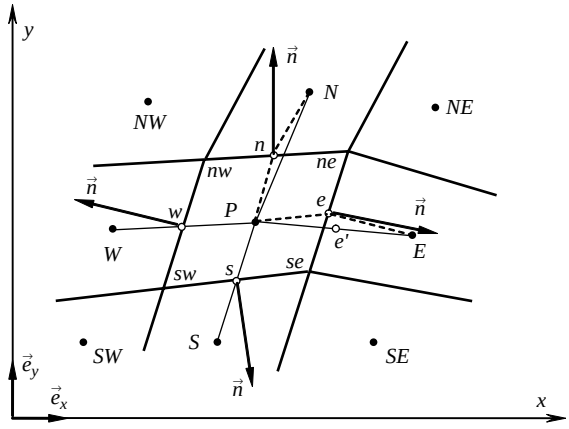

Figure 2.
A typical two-dimensional control volume

$$F_e^d = \mu_e \mathbf{S}_e \frac{\varphi_E - \varphi_P}{L_{PE}} + \mu_e \mathbf{S}_e \overline{(\mathrm{grad}\varphi)_e}^{\mathrm{Old}} \cdot \left(\vec{n} - \vec{i}_\xi\right) \tag{12}$$

where L_{PE} stands for the distance between P and E; $\vec{i}_\xi$ is the unit vector in the ξ-direction.

The different methods to approximate the value of φ and its derivative at the cell face result in different interpolation schemes. In the present study, the central difference scheme is used. Then the cell-face values of the variables are approximated as:

$$\varphi_e \approx \varphi_{e'} = \lambda_e \varphi_E + (1 - \lambda_e)\varphi_P \quad \text{for face } e \tag{13}$$

where the interpolation factor λ_e is defined as:

$$\lambda_e = \frac{|\vec{r}_e - \vec{r}_P|}{|\vec{r}_e - \vec{r}_P| + |\vec{r}_E - \vec{r}_e|} \tag{14}$$

where $\vec{r}_e$ is the position vector.

Equation (13) is a second-order approximation at the location e' on the straight line connecting nodes P and E (Figure 2). If the cell-face center e does not coincide with the location e', a correction term needs to be added in equation (13) to restore the second-order accuracy, which can be expressed as follows:

$$\varphi_e \approx \varphi_{e'} + \left(\mathrm{grad}\varphi\right)_{e'} \cdot \left(\vec{r}_e - \vec{r}_{e'}\right) \tag{15}$$

To obtain the deferred derivatives at the cell face, they are calculated first at the control volume centers and then interpolated to the cell faces. By using the Gauss' theorem, the derivative at the CV centers can be approximated by the average value over the cell:

$$\left(\frac{\partial \varphi}{\partial x_i}\right)_P \approx \frac{\int_\Omega \frac{\partial \varphi}{\partial x_i} \mathrm{d}\Omega}{\Delta\Omega} = \int_{\mathbf{S}} \varphi \vec{i}_i \cdot \vec{n} \mathrm{d}\mathbf{S} \approx \sum_c \varphi_c \mathbf{S}_c^i, \quad c = e, n, w, s \tag{16}$$

Then the cell-center derivatives can also be interpolated to the cell-face centers using the same interpolation as that described by equations (13)-(15).

The volume integral of the source term is:

$$Q_\varphi = \int_\Omega \mathbf{S}_\varphi \mathrm{d}\Omega \approx \mathbf{S}_\varphi \Delta\Omega \tag{17}$$

where Ω is the cell volume. For the unsteady source term, a three-level second order scheme is used:

$$\frac{\partial \varphi}{\partial t} = \frac{\left(3\varphi_p^n - 4\varphi_p^{n-1} + \varphi_p^{n-2}\right)}{2\Delta t} \tag{18}$$

where Δt is the time step, n is the time level. All the steady-state terms in the equations are discretized using the implicit scheme.

The momentum equations contain a contribution from the pressure. The volume integral of the pressure gradient term in u-momentum equation can be obtained by:

$$Q^{p}_{u,P} = \int_{\Omega} -\left(\frac{\partial p}{\partial x}\right)_P \mathrm{d}\Omega \approx -\left(\frac{\delta p}{\delta x}\right)_P \Delta\Omega \tag{19}$$

Then the final discrete form of the u-momentum equation is:

$$A^{u}_{P} u_P + \sum_{l} A^{u}_{l} u_l = Q^{*}_{u,P} - \left(\frac{\delta p}{\delta x}\right)_P \Delta\Omega \tag{20}$$

where P is the index of an arbitrary node; the index l denotes the four neighboring points E, W, S, N; the coefficients A^{φ}_{P}, A^{φ}_{E}, A^{φ}_{W}, A^{φ}_{N}, A^{φ}_{S} are those of the resultant algebraic equations; and $Q^{*}_{u,P}$ is the integral of the source term contributed by other forces.

In the present study, SIMPLEC method, developed by van Doormal and Raithby (1984) is applied to couple the velocity and pressure. To avoid oscillations in the pressure or velocity, the interpolation proposed by Rhie and Chow (1983) is adopted:

$$u^{m}_{e} = \overline{(u^{m})}_{e} - \Delta\Omega_e \overline{\left(\frac{1}{A^{u}_{P} + \sum_{l} A^{u}_{l}}\right)_e} \left[\left(\frac{\delta p}{\delta x}\right)_e - \overline{\left(\frac{\delta p}{\delta x}\right)_e}\right]^{m-1} \tag{21}$$

where m is integration step for each time level.

3.2 Porous medium region

Equations (3) and (4) recover the standard Navier-Stokes equations when the porosity approaches unity. Thus, the discretizing procedure for porous medium is similar to that for the homogenous fluid as the two sets of governing equations are similar in form. The discretized diffusion flux is similar in form to equation (13). The convective flux at a cell face is similar in form to equation (9) except for a small change:

$$F^{c}_{e} = \int_{\mathbf{S}_e} \frac{\rho u}{\varepsilon} \vec{u} \cdot \vec{n} \mathrm{d}\mathbf{S} \approx \frac{m_e u_e}{\varepsilon_e} \tag{22}$$

The volume integral of the pressure gradient term (similar in form to equation (18)) is:

$$Q^{p*}_{u,P} = \int_{\Omega} -\left(\frac{\partial(\varepsilon p^{*})}{\partial x}\right)_P \mathrm{d}\Omega \approx -\left(\varepsilon \frac{\delta p}{\delta x}\right)_P \Delta\Omega \tag{23}$$

For the Darcy term in equation (4), the volume integral can be expressed as:

$$Q^{u}_{D} = \int_{\Omega} -\left(\frac{\mu\varepsilon}{K} u\right)_p \mathrm{d}\Omega = -\left(\frac{\mu\varepsilon}{K}\right)_p \Delta\Omega \cdot u_p \tag{24}$$

For the Forchheimer term, the volume integral is given by:

$$Q^{u}_{F} = \int_{\Omega} -\left(\frac{\rho\varepsilon C_F \sqrt{u^2 + v^2}}{\sqrt{K}} u\right)_p \mathrm{d}\Omega = -\left(\frac{\rho\varepsilon C_F \sqrt{u^2 + v^2}}{\sqrt{K}}\right)_p \Delta\Omega \cdot u_p \tag{25}$$

It is convenient to treat the Darcy and Forchheimer terms as source terms. However, equations (24) and (25) indicate that, after integrating, both terms become a product of

Darcy velocity component and a coefficient. The two coefficients can be added into the coefficients of the algebraic equation A_p^u, which will accelerate the convergence rate.

The procedure to obtain the pressure correction equation is also similar to that for homogenous fluid (equation (21)), except for a small change:

$$u_e^m = \overline{(u^m)}_e - \Delta\Omega_e \overline{\left(\frac{1}{A_P^u + \sum_l A_l^u}\right)}_e \left[\left(\frac{\delta(\varepsilon p^*)}{\delta x}\right)_e - \overline{\left(\frac{\delta(\varepsilon p^*)}{\delta x}\right)}_e\right]^{m-1} \tag{26}$$

3.3 Interface treatment

In some cases, structured grids are difficult, even impossible, to construct for complex geometries. Therefore, in the present study, multi-block grids method is applied to provide a compromise between the simplicity and wide variety of solvers available for structured grids and ability to handle complex geometries that unstructured grids allow.

Figure 3 shows details of the interface between two different blocks. Two neighboring control volumes, lying in Blocks A and B, respectively, share the interface. The grids in two neighboring blocks match at the interface. The treatment for fluid – porous medium interface is shown here.

Blocks A and B (Figure 3) represent fluid and porous medium, respectively. The velocity vector at the interface is given by $\vec{v}_{\text{Interface}}$. It can be written in either the *x-y* or *n-t* coordinate systems as:

$$\vec{v}_{\text{Interface}} = u\vec{e}_x + v\vec{e}_y = u_n\vec{n} + u_t\vec{t} \tag{27}$$

where u and v are the components of $\vec{v}_{\text{Interface}}$ in the x and y directions; u_n and u_t are the $\vec{v}_{\text{Interface}}$ components along n and t directions, respectively; $\vec{e}_x$, $\vec{e}_y$, $\vec{n}$ and $\vec{t}$ are the unit vectors along x, y, normal and tangential directions.

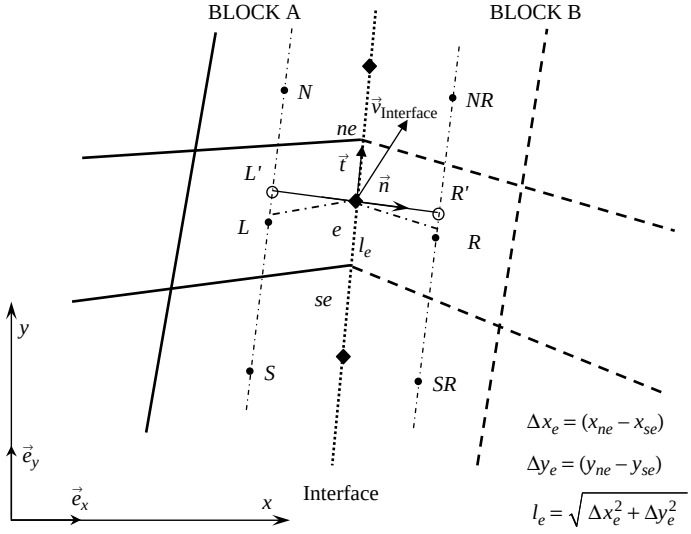

Figure 3.
Interface between two blocks with matching grids

The component u_t then can be written as:

$$u_t = u\vec{e}_x \cdot \vec{t} + v\vec{e}_y \cdot \vec{t} \tag{28}$$

By combining equations (5), (7) and (27):

$$\frac{\mu}{\varepsilon}\left.\frac{\partial \vec{v}_{\text{Interface}}}{\partial n}\right|_{\text{Porous}} - \mu\left.\frac{\partial \vec{v}_{\text{Interface}}}{\partial n}\right|_{\text{Fluid}} = \beta\frac{\mu}{\sqrt{K}}\,u_t\vec{t} + \beta_1\rho u_t^2\vec{t} \tag{29}$$

The unit vector ($\vec{t}$) parallel to the interface (Figure 2) is calculated from:

$$\vec{t} = \frac{(x_{ne} - x_{se})\vec{e}_x + (y_{ne} - y_{se})\vec{e}_y}{\sqrt{(x_{ne} - x_{se})^2 + (y_{ne} - y_{se})^2}} = \frac{\Delta x_e\vec{e}_x + \Delta y_e\vec{e}_y}{l_e} \tag{30}$$

By substituting the components of $\vec{v}_{\text{Interface}}$ in the x and y directions, the equation (29) becomes:

$$\frac{\mu}{\varepsilon}\left.\frac{\partial u}{\partial n}\right|_{\text{Porous}} - \mu\left.\frac{\partial u}{\partial n}\right|_{\text{Fluid}} = \beta\frac{\mu}{\sqrt{K}}\,\frac{u\Delta x_e\Delta x_e + v\Delta y_e\Delta x_e}{l_e^2} + \beta_1\rho\frac{\Delta x_e(u\Delta x_e + v\Delta y_e)^2}{l_e^3} \tag{31}$$

$$\frac{\mu}{\varepsilon}\left.\frac{\partial v}{\partial n}\right|_{\text{Porous}} - \mu\left.\frac{\partial v}{\partial n}\right|_{\text{Fluid}} = \beta\frac{\mu}{\sqrt{K}}\,\frac{u\Delta x_e\Delta y_e + v\Delta y_e\Delta y_e}{l_e^2} + \beta_1\rho\frac{\Delta y_e(u\Delta x_e + v\Delta y_e)^2}{l_e^3} \tag{32}$$

The derivatives at the interface are calculated from the values at auxiliary nodes L' and R'; these nodes lie at the intersection of the cell face normal n and straight lines connecting nodes L and N or R and NR, respectively, as shown in Figure 3. The normal gradients at the interface can be calculated by using the first order difference approximation:

$$\left.\frac{\partial u}{\partial n}\right|_{\text{Porous}} = \frac{u|_{R'} - u|_e}{L_{eR'}}, \quad \left.\frac{\partial v}{\partial n}\right|_{\text{Porous}} = \frac{v|_{R'} - v|_e}{L_{eR'}} \tag{33}$$

$$\left.\frac{\partial v}{\partial n}\right|_{\text{Fluid}} = \frac{v|_e - v|_{L'}}{L_{L'e}}, \quad \left.\frac{\partial v}{\partial n}\right|_{\text{Fluid}} = \frac{v|_e - v|_{L'}}{L_{L'e}} \tag{34}$$

The Cartesian velocity components at L' and R' can be calculated by using bilinear interpolation or by using the gradient at the control volume center:

$$u|_{L'} = u|_L + (\text{grad}u)_L \cdot \vec{L'L} \tag{35}$$

To obtain higher order approximation of the derivatives, the velocity components at more auxiliary nodes may be needed. Alternatively, the shape functions may be used, which produces a kind of combined finite element/finite volume method for calculating the higher order approximations.

By using equations (31)-(35) and explicitly calculating the terms at the right hand sides of equations (31) and (32), the Cartesian velocity components u and v at the interface are obtained. Then the convective fluxes at the interface can be calculated. The diffusive fluxes are calculated from equations (33)-(35). Then the coefficients A_L and A_R can be obtained.

To close the algebra equation system, the pressure at the interface must be determined. However, Betchen *et al.* (2006) pointed out that the pressure gradient at the interface may not be continuous due to the rather large Darcy and Forchheimer terms (equation (4)), which may result in a rapid pressure drop at the porous side. This discontinuity of the pressure gradient becomes more severe at higher Reynolds number and lower Darcy number. Thus, it requires special treatment to estimate the interface pressure from that of the vicinity at either side. A simplistic pressure estimation may give unrealistic, oscillatory velocity profile. The coupling issue of pressure-velocity at the interface was described in a recent paper by Betchen *et al.* (2006) who proposed a solution that enables stable calculations. The pressure is extrapolated in the fluid side to a location at a small distance near the interface. From this location, a momentum balance is then used to estimate the interface pressure. This estimate is then averaged with the pressure extrapolated from the porous side to obtain the interface pressure. In the present paper, a less complex treatment was adopted. Extrapolations from the fluid and porous sides give two different estimates of the interface pressure. The average of the two estimates is used as the interface pressure. A small number of iterations is required for accuracy.

4. Results and discussion

The Reynolds number is based on the mean velocity and the height of the cylinder, $Re = \rho UH/\mu$, Darcy number is $Da = K/H^2$, and Forchheimer coefficient $C_F = 1.75/\sqrt{(150\varepsilon^3)}$, as used by Nithiarasu *et al.* (1999). Non-uniform, body-fitted and non-orthogonal meshes are employed, where the density of meshes around the cylinder is larger than those areas far away (Figure 1(b)). At the left boundary, the incoming flow is uniform, and at the other three boundaries, $\partial u/\partial n = 0$. The initial conditions for the computation were either uniform flow at the inlet or the results of a previous calculation, often at different Reynolds number, Darcy number or porosity values. The time step is set equal to 10^{-2}, and the convergence criteria for each time level is set as follows:

$$\frac{\sum \varphi_{i,j}^{m+1} - \varphi_{i,j}^{m}}{\left|\sum \varphi_{i,j}^{m+1} \leq \varepsilon_c\right|} \tag{36}$$

where $\varepsilon_c = 10^{-6}$.

To validate the present program, the drag and lift coefficients for the flow around a circular cylinder are compared with those in previous studies. The results shown in Table I agree well with the benchmark studies. Considering the computational cost and accuracy, a grid independency check (details not shown) shows that a 240 × 120 mesh is enough for use in subsequent computations.

	$Re = 100$		$Re = 200$	
	C_D	C_L	C_D	C_L
Braza *et al.* (1986)	1.36±0.015	±0.250	1.40±0.050	±0.75
Liu *et al.* (1998)	1.35±0.012	±0.339	1.31±0.049	±0.69
Calhoun (2002)	1.33±0.014	±0.298	1.17±0.058	±0.67
Present	1.38±0.009	±0.335	1.36±0.050	±0.73

Table I. Comparison of drag and lift coefficients with previous studies

Figure 4 shows the instantaneous streamlines for different Reynolds number, at constant porosity $\varepsilon = 0.4$, Darcy number $Da = 10^{-4}$, jump coefficients $\beta = 0$ and $\beta_1 = 0$. The flow phenomenon of this case is like those of the non-porous one. As the $Re = 20$, a closed steady recirculation region consisting of twin symmetric vortices forms behind the cylinder. This recirculation region increases in size with the increase in Reynolds number, shown as $Re = 40$. When the Reynolds number becomes larger, the flow becomes unsteady; the vortices in the separation bubble start to separate

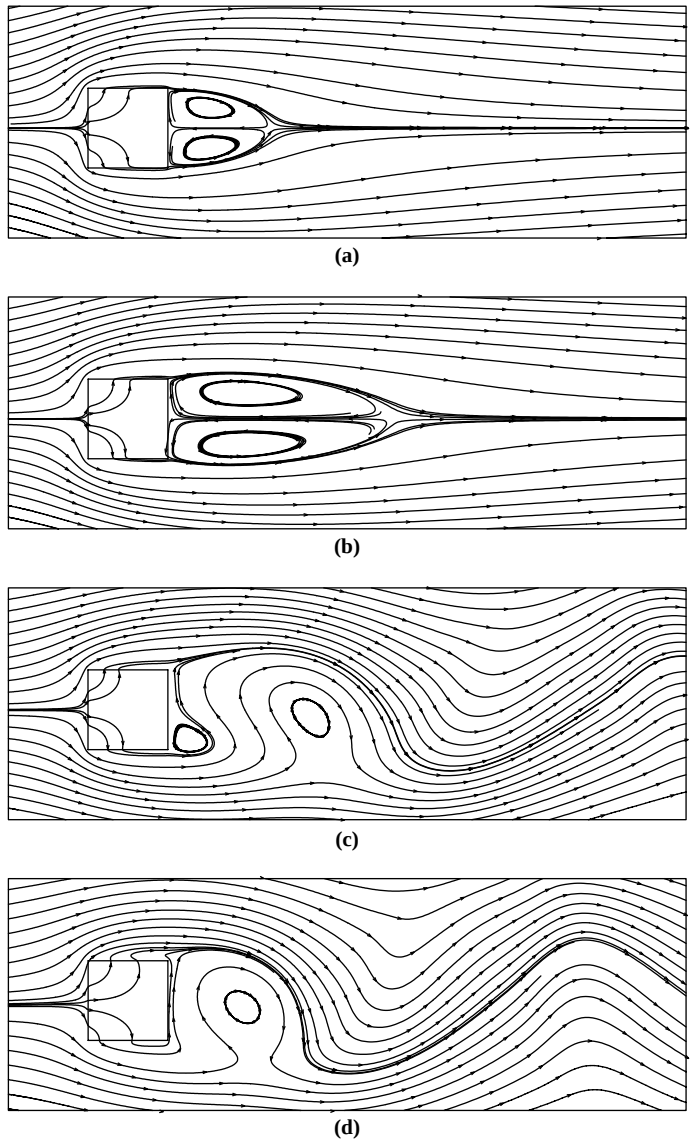

Figure 4.
Instantaneous streamline contours at $\varepsilon = 0.4$, $Da = 10^{-4}$ and $\beta = 0$, $\beta_1 = 0$. (a) $Re = 20$; (b) $Re = 40$; (c) $Re = 100$; (d) $Re = 200$

alternatively from the trailing edge of the square cylinder and move downstream, which is the vortex shedding phenomena. Owing to the permeability characteristic of the porous media, the shedding intensity would be less than that in solid one, and the critical Reynolds number, where the flow changes to unsteady from steady, is less than that in solid one.

Figure 5 shows out the instantaneous streamline contours for different Darcy number at $\varepsilon = 0.4$, $Re = 20$ and $\beta = 0$, $\beta_1 = 0$. It can be seen that when $Da = 10^{-2}$,

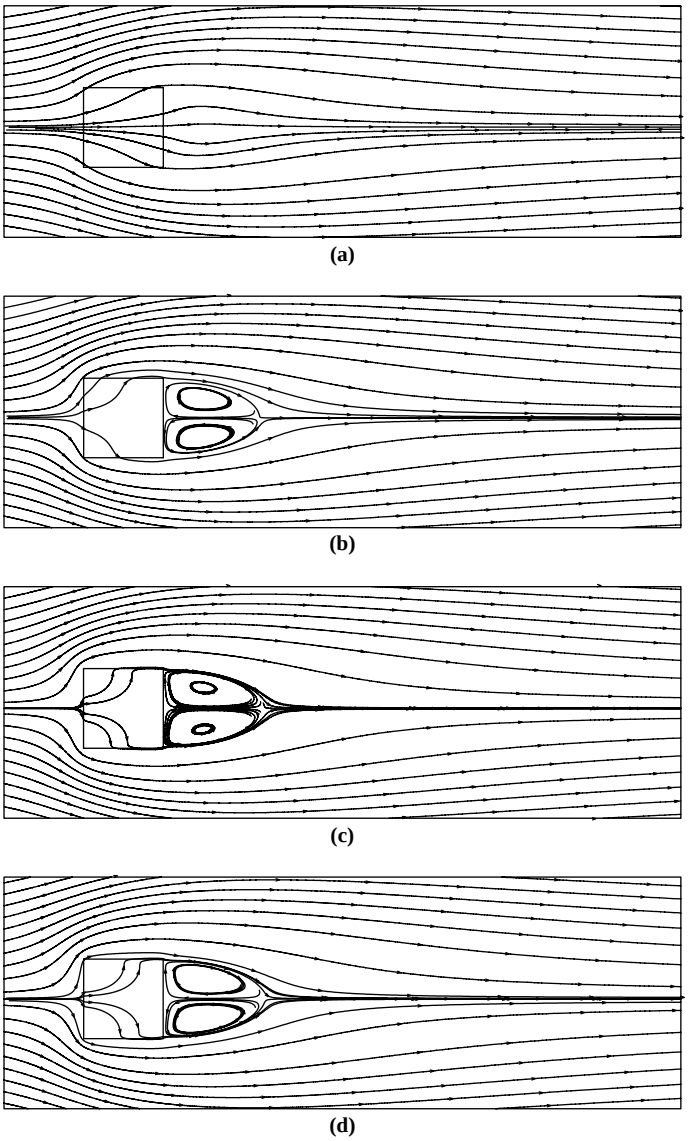

Figure 5.
Instantaneous streamline contours at $\varepsilon = 0.4$, $Re = 20$ and $\beta = 0$, $\beta_1 = 0$. (a) $Da = 10^{-2}$; (b) $Da = 10^{-3}$; (c) $Da = 10^{-4}$; (d) $Da = 10^{-5}$

there is no vortex formation behind the cylinder. When Da decreases from 10^{-3} to 10^{-5}, as less fluid flows through the cylinder, the vortex is formed and its circulation length is increased. The flow filed resembles that around a solid cylinder, when Da approaches zero.

Figure 6 shows the drag and lift coefficient history development, for $Re = 200$, $\varepsilon = 0.4$, $Da = 10^{-4}$ and $\beta = 0$, $\beta_1 = 0$. They show that the unsteady vortex shedding becomes periodic, and the frequency of lift coefficient is twice of drag coefficient, which are consistent with those of solid ones (Davis and Moore, 1982). Figure 7 shows this periodic characteristic streamline contour in one period. It is shown that, different from the solid one, the wake flow coming backwards may penetrate into the porous cylinder. However, at $Re = 250$, for the drag coefficient shown in Figure 8, it is not a simple sine wave and there seems to be a small modulation in shedding frequency. This kind of phenomena was also found for the solid case by Davis and Moore (1982), which is out of the scope of the present study. So in the following study, the Re ranges from 20 to 200.

Table II shows the influence of the stress jump parameters β and β^1 at the lower Reynolds numbers $Re = 20$ and 40, with $\varepsilon = 0.4$ and $Da = 10^{-4}$. When $Re = 20$, the β effect is noticeable, whereas β_1 has less effect. From equation (5), if the permeability K is small, that is Darcy number is small, the viscous term $\beta(\mu/\sqrt{K})u_t$ is large. An interesting phenomenon is that when $Re = 40$, for different combinations of β and β_1, the flow would become steady or unsteady. The instability at low Re is unexpected and may be caused by the sudden large stress jump at the interface. Figure 9 shows the instantaneous stream contours for these stress jump interface conditions. By checking the stream contours in one periodic time, it is found that the two vortices are not shed from the cylinder, but its size alternate periodically from small to large. This observation shows the importance of the stress jump boundary conditions. The stress jump parameters β and β^1 are empirical inputs dependent on the porous medium

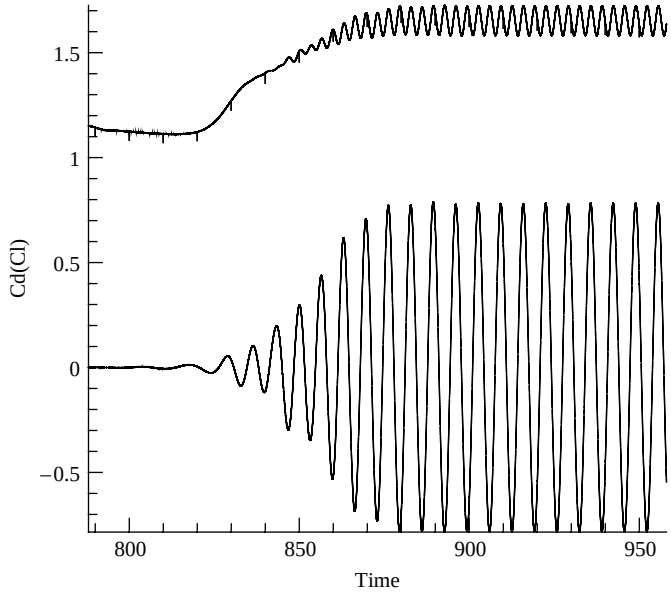

Figure 6.
Drag (up) and lift (down) coefficient histories, at $Re = 200$, $\varepsilon = 0.4$, $Da = 10^{-4}$ and $\beta = 0$, $\beta_1 = 0$

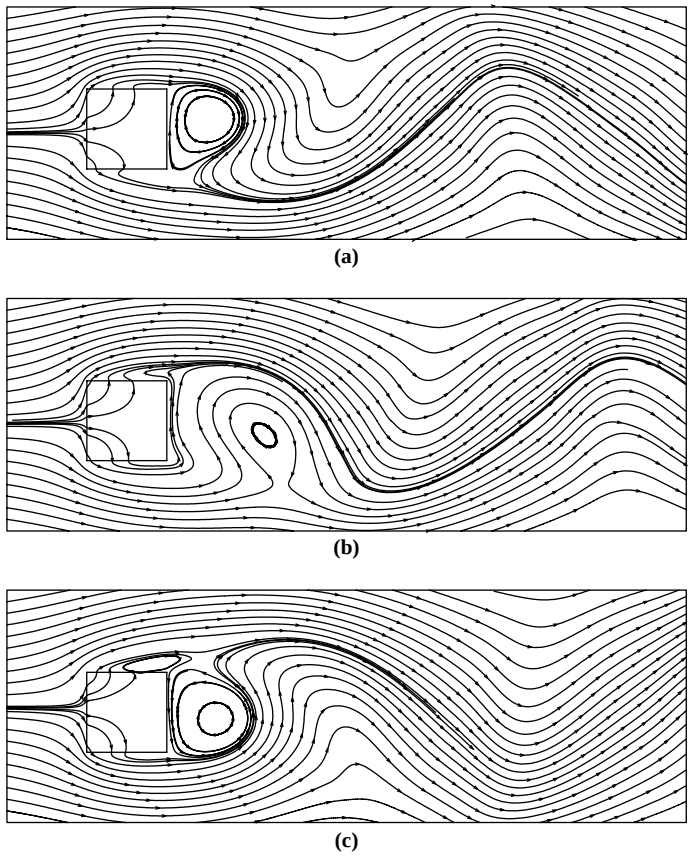

Figure 7.
Streamline contours at $Re = 200$, $\varepsilon = 0.4$, $Da = 10^{-4}$ and $\beta = 0$, $\beta_1 = 0$, (a) $C_L = \max$; (b) $C_L = 0$; (c) $C_L = \min$

properties as discussed in Section 2. In the numerical model these boundary parameters will determine the flow of fluid into as well as out of the porous medium; and the differences in bleed flow may have caused the changes in the vortex formation. Note that β and β_1 are not numerical stability parameters which need to be optimized.

Table III shows the influence of the stress jump parameters β and β_1 at the higher Reynolds numbers $Re = 100$, and 200, with $\varepsilon = 0.4$ and $Da = 10^{-4}$. It can be seen that for the same Reynolds number, β effect is still more obvious than β_1. Yu *et al.* (2007) showed that the viscous term $\beta(\mu/\sqrt{k})u_t$ effect dominates for $Re = 20$, and suggested that the inertial term $\beta_1 \rho u_t^2$, in equation (5), may be important at high Reynolds number. However, the Reynolds number in the present study was not increased above 200 to avoid the complications from 3D flow and the frequency modulation noted above.

Table III also shows in greater detail the effect of β and β_1 for $Re = 200$, respectively. It can be seen that when β increases from -0.7 to 0.7, the average drag coefficient, and the amplitude of both lift and drag coefficients shows a decreasing trend; but for the shedding period, there is no consistent trend. When β_1 increases from -0.7 to 0.7, the change is not large. This shows that in equation (5), the viscous term $\beta(\mu/\sqrt{k})u_t$ is more important than the inertial term $\beta_1 \rho u_t^2$.

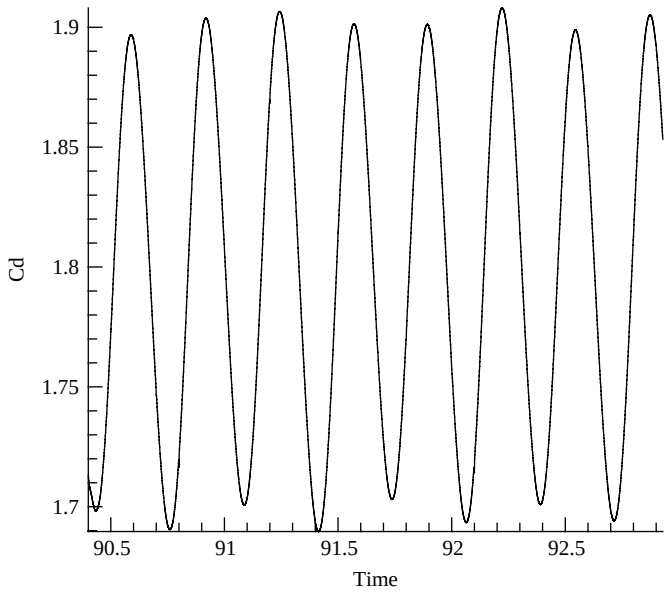

Figure 8.
Periodic drag coefficient histories, at $Re = 250$, $\varepsilon = 0.4$, $Da = 10^{-4}$ and $\beta = 0.7$, $\beta_1 = 0$

Re	β	β_1	C_D	*L*/*H*
20	−0.7	0	1.991	1.23
	0	0	2.411	1.26
	0.7	0	2.550	1.27
	0	−0.7	2.376	1.26
	0	0	2.411	1.26
	0	0.7	2.371	1.26
40	−0.7	0	1.448-1.463	–
	0	0	1.611	2.77
	0.7	0	1.534-1.568	–
	0	−0.7	1.502-1.539	–
	0	0	1.611	2.77
	0	0.7	1.611	2.76

Table II.
Drag coefficient and length of the recirculation zone, for low *Re*, with $\varepsilon = 0.4$, and $Da = 10^{-4}$

Table IV shows the influence of Darcy number. For the steady cases, $Re = 20$ and 40, the drag coefficient and length of recirculation zone decreases when the Darcy number increases. This is due to more porous flow. It can be seen that the results for $Da = 10^{-4}$ and 10^{-5} changes little, as for $Da \leq 10^{-4}$, the flow inside the porous media is rather small, called Darcy flow conventionally. For $Re = 100$, it is interesting to find that the flow is still steady when $Da = 10^{-2}$. For the unsteady cases, $Re = 100$ and 200, there is no clear trend arising from Darcy number. The flow is more complicated because the porous flow may affect the location of the streamline separation near the back edge of the square cylinder (see instantaneous streamlines in Figure 4).

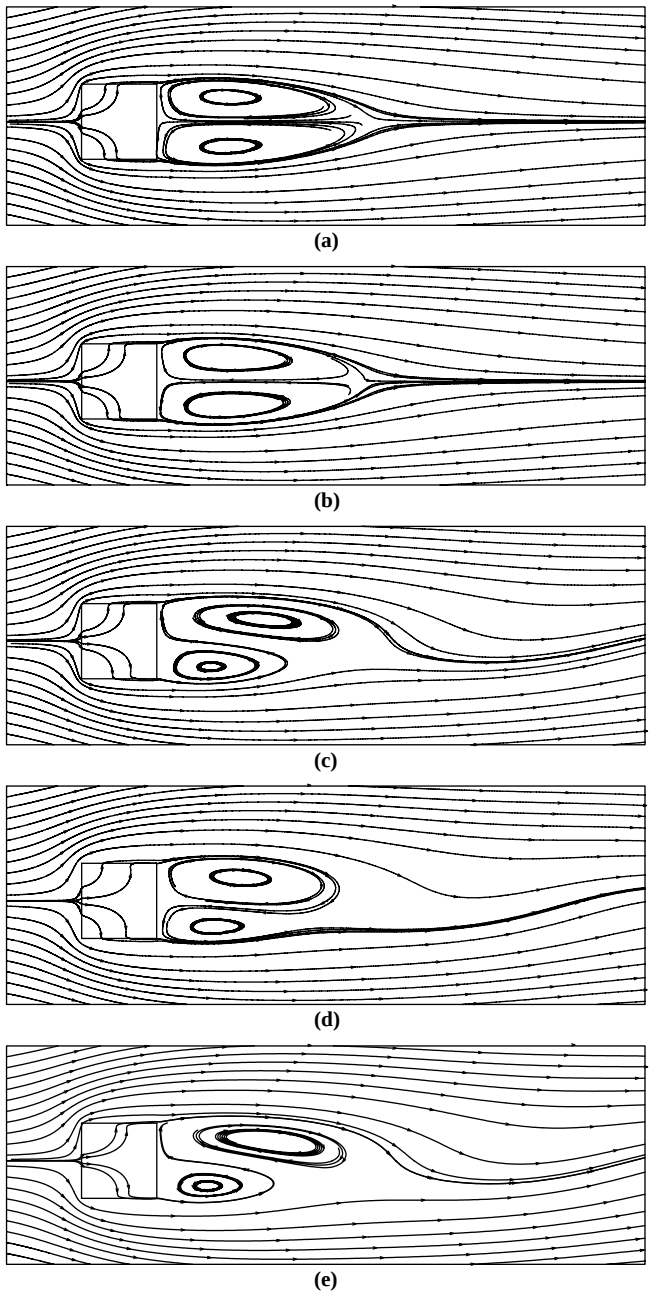

Figure 9.
Instantaneous streamline contours at $Re = 40$, $\varepsilon = 0.4$, $Da = 10^{-4}$. (a) $\beta = 0$, $\beta_1 = 0$; (b) $\beta = 0$, $\beta_1 = 0.7$; (c) $\beta = 0$, $\beta_1 = -0.7$; (d) $\beta = 0.7$, $\beta_1 = 0$; (e) $\beta = -0.7$, $\beta_1 = 0$

Re	β	β_1	τ_p	C_L	C_D (amplitude)
100	0	0.7	6.97	−0.265-0.265	1.432-1.447 (0.015)
	0	0	6.94	−0.269-0.269	1.433-1.448 (0.015)
	0	−0.7	7.08	−0.266-0.266	1.431-1.447 (0.016)
	0.7	0	6.93	−0.264-0.264	1.441-1.457 (0.016)
	0	0	6.94	−0.269-0.269	1.433-1.448 (0.015)
	−0.7	0	7.02	−0.270-0.270	1.417-1.432 (0.015)
200	0	0.7	6.63	−0.788-0.788	1.585-1.730 (0.145)
	0	0.5	6.59	−0.783-0.783	1.584-1.726 (0.142)
	0	0.3	6.60	−0.782-0.782	1.583-1.725 (0.142)
	0	0	6.60	−0.782-0.782	1.581-1.722 (0.141)
	0	−0.3	6.61	−0.783-0.783	1.581-1.724 (0.143)
	0	−0.5	6.66	−0.785-0.785	1.582-1.726 (0.144)
	0	−0.7	6.63	−0.787-0.787	1.584-1.731 (0.147)
	0.7	0	6.62	−0.759-0.759	1.568-1.706 (0.138)
	0.5	0	6.64	−0.765-0.765	1.571-1.710 (0.139)
	0.3	0	6.62	−0.770-0.770	1574-1.714 (0.140)
	0	0	6.60	−0.782-0.782	1.581-1.722 (0.141)
	−0.3	0	6.60	−0.799-0.799	1.593-1.736 (0.143)
	−0.5	0	6.67	−0.816-0.816	1.604-1.750 (0.146)
	−0.7	0	6.53	−0.840-0.840	1.621-1.771 (0.150)

Table III.
Drag, lift and period for high *Re* with unsteady vortex shedding, with $\varepsilon = 0.4$, and $Da = 10^{-4}$

Re	*Da*	τ_p	C_L	C_D(amplitude)	*L*/*H*
20	10^{-5}	–	0	2.413	1.32
	10^{-4}	–	0	2.411	1.26
	10^{-3}	–	0	2.143	1.21
	10^{-2}	–	0	1.974	–
40	10^{-5}	–	0	1.616	2.81
	10^{-4}	–	0	1.611	2.77
	10^{-3}	–	0	1.535	2.66
	10^{-2}	–	0	1.472	–
100	10^{-5}	7.15	−0.225-0.225	1.284-1.293 (0.009)	–
	10^{-4}	6.94	−0.269-0.269	1.433-1.448 (0.015)	–
	10^{-3}	7.10	−0.262-0.262	1.638-1.658 (0.020)	–
	10^{-2}	–	0	1.096	–
200	10^{-5}	6.43	−0.546-0.546	1.343-1.418 (0.075)	–
	10^{-4}	6.60	−0.782-0.782	1.581-1.722 (0.141)	–
	10^{-3}	6.23	−0.310-0.310	1.634-1.816 (0.182)	–
	10^{-2}	6.52	−0.212-0.212	1.064-1.288 (0.224)	–

Table IV.
Effect of porosity with $Da = 10^{-4}$ and $\beta = 0, \beta_1 = 0$

Table V shows that at higher porosity, there is decrease of drag coefficient (average for unsteady cases). For the unsteady cases the lift amplitude is smaller at higher porosity. This behavior may be explained by the effect of more porous flow through the cylinder. There are not much effect of porosity on recirculation length and shedding period. However, the effect of porosity is smaller than that of Darcy number which is consistent with the observation of Jue (2004).

Re	ε	τ_p	C_L	C_D (amplitude)	L/H
20	0.4	–	0	2.411	1.26
	0.6	–	0	2.105	1.24
	0.8	–	0	2.049	1.25
40	0.4	–	0	1.611	2.73
	0.6	–	0	1.584	2.69
	0.8	–	0	1.537	2.71
100	0.4	6.94	−0.269-0.269	1.433-1.448 (0.015)	–
	0.6	7.06	−0.261-0.261	1.419-1.433 (0.014)	–
	0.8	7.02	−0.257-0.257	1.407-1.420 (0.013)	–
200	0.4	6.60	−0.782-0.782	1.581-1.722 (0.141)	–
	0.6	6.55	−0.772-0.772	1.575-1.715 (0.140)	–
	0.8	6.49	−0.750-0.750	1.563-1.698 (0.135)	–

Table V.
Effect of Darcy number with $\varepsilon = 0.4$, $\beta = 0$, and $\beta_1 = 0$

5. Conclusion

The two-dimensional flow around a porous square cylinder has been carried out numerically using finite volume method, based on the body-fitted, non-orthogonal grids, and multi-block technology. This treatment of a simple geometry with body-fitted and multi-block grids has the advantage that it may be extended to more complex geometries like the flow past several square cylinders. The flow in porous region is described by the generalized Darcy-Brinkman-Forchheimer extended model, which considers the inertia, convective, and viscous effects.

The flow range considered was varied from steady state to unsteady Reynolds number 200, and different porosity, Darcy number and stress jump parameters were considered. With a larger Darcy number, the Reynolds number has to be higher before the vortex shedding phenomena occurs. The results also show that the interface stress jump parameters play an important role in the stability of the flow around a porous square cylinder. The effects of the stress jump parameters, β and β_1 ranging from -0.7 to 0.7, are given for the flow condition from $Re = 20$ to 200. The first coefficient β has a more noticeable effect whereas the second coefficient β_1 has small effect, even for $Re = 200$. Generally, a larger porosity cylinder results in a smaller drag coefficient and shedding period. The Darcy number effect becomes smaller when $Da \leq 10^{-4}$; at larger Darcy number, the fluctuation-amplitude of drag coefficient increases.

References

Alazmi, B. and Vafai, K. (2001), "Analysis of fluid flow and heat transfer interfacial conditions between a porous medium and a fluid layer", *Int. J. Heat Mass Transfer*, Vol. 44, pp. 1735-49.

Beavers, G.S. and Joseph, D.D. (1967), "Boundary conditions at a natural permeable wall", *J. Fluid Mech.*, Vol. 30, pp. 197-207.

Betchen, L., Straatman, A.G. and Thompson, B.E. (2006), "A nonequilibrium finite-volume model for conjugate fluid/porous/solid domains", *Numer. Heat Transfer A*, Vol. 49, pp. 543-65.

Braza, M., Chassaing, P. and Ha Minh, H. (1986), "Numerical study and physical analysis of the pressure and velocity fields in the near wake of a circular cylinder", *J. Fluid. Mech.*, Vol. 165, pp. 79-130.

Calhoun, D. (2002), "A Cartesian grid method for solving the two-dimensional streamfunction-vorticity equations in irregular regions", *J. Comput. Phy.*, Vol. 176, pp. 231-75.

Cohen, R.D. (1991), "Predicting the effects of surface suction and blowing on the strouhal frequencies in vortex shedding", *JSME International Journal (Series II)*, Vol. 34, pp. 30-9.

Costa, V.A.F., Oliveira, L.A., Baliga, B.R. and Sousa, A.C.M. (2004), "Simulation of coupled flows in adjacent porous and open domains using a control-volume finite-element method", *Numer. Heat Transfer A*, Vol. 45, pp. 675-97.

Davis, R.W. and Moore, E.F. (1982), "A numerical study of vortex shedding from rectangles", *J. Fluid Mech.*, Vol. 116, pp. 475-506.

Davis, R.W., Moore, E.F. and Purtell, L.P. (1984), "A numerical-experimental study of confined flow around rectangular cylinders", *Phys. Fluids*, Vol. 27 No. 1, pp. 46-59.

Ferziger, J.H. and Perić, M. (1999), *Computational Methods for Fluid Dynamics*, 2nd ed., Springer, Berlin, pp. 222-33.

Franke, R., Rodi, W. and Schönung, B. (1990), "Numerical calculation of laminar vortex shedding past cylinders", *J. Wind Eng. Ind. Aerodyn.*, Vol. 35, pp. 237-57.

Gartling, D.K., Hickox, C.E. and Givler, R.C. (1996), "Simulation of coupled viscous and porous flow problems", *Comp. Fluid Dyn.*, Vol. 7, pp. 23-48.

Hsu, C.T. and Cheng, P. (1990), "Thermal dispersion in a porous medium", *Int. J. Heat Mass Transfer*, Vol. 33, pp. 1587-97.

Huang, P.C. and Vafai, K. (1993), "Flow and heat transfer control using a porous block array arrangement", *Int. J. Heat Mass Transfer*, Vol. 36, pp. 4019-32.

Jue, T.C. (2004), "Numerical analysis of vortex shedding behind a porous cylinder", *Int. J. Numer. Methods Heat Fluid Flow*, Vol. 14, pp. 649-63.

Kim, S.J. and Choi, C.Y. (1996), "Convection heat transfer in porous and overlying layers heated from below", *Int. J. Heat Mass Transfer*, Vol. 39, pp. 319-29.

Klekar, K.M. and Patankar, S.V. (1992), "Numerical predication of vortex shedding behind square cylinders", *Int. J. Numer. Meth. Fluid*, Vol. 14, pp. 327-41.

Ling, L.M., Ramaswamy, B., Cohen, D.R. and Jue, T.C. (1993), "Numerical analysis on Strouhal frequencies in vortex shedding over square cylinders with surface suction and blowing", *International Journal of Numerical Methods for Heat and & Fluid Flow*, Vol. 3, pp. 458-67.

Liu, C., Sheng, X. and Sung, C.H. (1998), "Preconditioned multigrid methods for unsteady incompressible flows", *J. Comput. Phys.*, Vol. 139, pp. 35-57.

Martin, A.R., Saltiel, C. and Shyy, W. (1998), "Heat transfer enhancement with porous inserts in recirculating flows", *J. Heat Transfer*, Vol. 120, pp. 458-67.

Muzaferija, S. (1994), "Adaptive finite volume method for flow predictions using unstructured meshes and multigrid approach", PhD thesis, University of London, London.

Neale, G. and Nader, W. (1974), "Practical significance of Brinkman's extension of Darcy's law: coupled parallel flows within a channel and a bounding porous medium", *Can. J. Chem. Engrg.*, Vol. 52, pp. 475-8.

Nithiarasu, P., Seetharamu, K.N. and Sundararajan, T. (2002), "Finite element modelling of flow, heat and mass transfer in fluid saturated porous media", *Arch. Comput. Meth. Engng*, Vol. 9, pp. 3-42.

Nithiarasu, P., Sujatha, K.S., Sundararajan, T. and Seetharamu, K.N. (1999), "Buoyancy driven flow in a non-Darcian, fluid-saturated porous enclosure subjected to uniform heat flux – a numerical study", *Commun. in Nume. Meth. Engng*, Vol. 15, pp. 765-76.

Ochoa-Tapia, J.A. and Whitaker, S. (1995a), "Momentum transfer at the boundary between a porous medium and a homogeneous fluid I: theoretical development", *Int. J. Heat Mass Transfer*, Vol. 38, pp. 2635-46.

Ochoa-Tapia, J.A. and Whitaker, S. (1995b), "Momentum transfer at the boundary between a porous medium and a homogeneous fluid II: comparison with experiment", *Int. J. Heat Mass Transfer*, Vol. 38, pp. 2647-55.

Ochoa-Tapia, J.A. and Whitaker, S. (1998), "Momentum jump condition at the boundary between a porous medium and a homogeneous fluid: inertial effect", *J. Porous Media*, Vol. 1, pp. 201-17.

Rhie, C.M. and Chow, W.L. (1983), "Numerical study of the turbulent flow past an airfoil with trailing edge separation", *AAIA J.*, Vol. 21, pp. 1525-32.

Silva, R.A. and de Lemos, M.J.S. (2003), "Numerical analysis of the stress jump interface condition for laminar flow over a porous layer", *Numer. Heat Transfer A*, Vol. 43, pp. 603-17.

Suzuki, H., Inoue, Y., Nishimura, T., Fukutani, F. and Suzuki, K. (1993), "Unsteady flow in a channel obstructed by a square rod (crisscross motion of vortex)", *Int. J. Heat Fluid Flow*, Vol. 14 No. 1, pp. 2-9.

Vafai, K. and Kim, S.J. (1990), "Fluid mechanics of the interface region between a porous medium and a fluid layer – an exact solution", *Int. J. Heat Fluid Flow*, Vol. 11, pp. 254-6.

van Doormal, J.P. and Raithby, G.D. (1984), "Enhancements of the SIMPLE method for predicting incompressible fluid flows", *Numer. Heat Transfer*, Vol. 7, pp. 147-63.

Williamson, C.H.K. (1996), "Vortex dynamics in the cylinder wake", *Annu. Rev. Fluid Mech.*, Vol. 28, pp. 477-539.

Yu, P., Lee, T.S., Zeng, Y. and Low, H.T. (2007), "A numerical method for flows in porous and homogenous fluid domains coupled at the interface by stress jump", *Int. J. Numer. Meth. Fluids*, Vol. 53, pp. 1755-75.

Zdravkovich, M.M. (1997), *Flow Around Circular Cylinders, Vol. 1: Fundamentals*, Oxford University Press, New York, NY.

Corresponding author
Hong-Tong Low can be contacted at: mpelowht@nus.edu.sg